A&A 411, 109–121 (2003)
DOI: 10.1051/0004-6361:20031297
© ESO 2003

Astronomy & Astrophysics

High resolution 21 cm mapping of the Ursa Major Galactic cirrus: Power spectra of the high-latitude HI gas

M.-A. Miville-Deschênes[1,2], G. Joncas[3], E. Falgarone[4], and F. Boulanger[1]

[1] Institut d'Astrophysique Spatiale, Université Paris-Sud, Bât. 121, 91405 Orsay, France
[2] Canadian Institute for Theoretical Astrophysics, 60 St-George st, Toronto, Ontario M5S 3H8, Canada
[3] Département de physique, de génie physique et d'optique, Observatoire du mont Mégantic, Université Laval, Sainte-Foy, Québec G1K 7P4, Canada
[4] LERMA/LRA, CNRS-UMR 8112, École Normale Supérieure, 24 rue Lhomond, 75005 Paris, France

Received 8 January 2003 / Accepted 1 July 2003

Abstract. We present a power spectrum analysis of interferometric 21 cm observations of the Ursa Major high-latitude cirrus, obtained with the Dominion Radio Astrophysical Observatory (DRAO) of Penticton (Canada). These high-resolution data reveal the intricate structure of the diffuse Galactic HI, at angular scales from 1 arcmin to 3 degrees. A filtering method based on a wavelet decomposition was used to enhance the signal-to-noise ratio of the data. The power spectra of the integrated emission and of the centroid velocity fields were used to deduce the three-dimensional (3D) spectral index of the density and velocity fields of the HI cirrus. The spectral index is similar for the 3D density and velocity fields with a value of -3.6 ± 0.2. Using the Leiden/Dwingeloo observations, this analysis was extended to the whole North Celestial Loop (which includes the Ursa Major cirrus), showing that the scaling laws prevail from 0.1 to 25 pc. The centroid velocity and integrated emission fields show moderate correlation, with a maximum cross-correlation value of 0.44.

Key words. ISM: general – radio lines: ISM

1. Introduction

It has been noted long ago (Chandrasekhar 1949; von Weizsäcker 1951) that the interstellar medium (ISM) has the dynamical properties of a turbulent flow. The high Reynolds number of the ISM has often been invoked to ascribe its self-similarity, observed with several tracers on scales from a few tenths to several hundreds of parsecs, to the presence of a fully developed turbulence. Nevertheless, despite the numerous efforts done to determine the dynamical properties of interstellar gas, the properties of interstellar turbulence are still poorly known. This is mainly due to the difficulty in deducing three-dimensional properties of the gas using projected quantities, but also to opacity effects and to the limited range of scales observed. Characterizing interstellar turbulence, by determining its statistical properties for instance, is still of major importance for the understanding of the structure and the kinematics of the ISM and its impact on the star formation process. In particular the statistical properties of the ISM structure and kinematics can be used to identify regions with exceptional dynamical properties and study their impact on the general evolution of the interstellar matter (see Falgarone & Phillips 1990; Falgarone et al. 1995; Joulain et al. 1998). For instance this is essential to characterize the dynamical conditions that favor the cooling and condensation of HI into its molecular form. The same is true for the fragmentation/coagulation of dust grains (Falgarone & Puget 1995). On the theoretical side, there is a need for observational constraints for the ISM statistical properties. These, like the power spectrum of density and velocity fluctuations in three dimensions (3D), would nicely complement the numerical simulation efforts that have been conducted lately (e.g. Porter et al. 1994; Stone et al. 1998; Mac Low 1999; Padoan & Nordlund 1999; Lazarian et al. 2001; Heitsch et al. 2001; Ostriker et al. 2001).

The statistical analysis of the information contained in line profiles is well suited for of such a study. Regarding the column density fluctuations, several studies have shown the self-similar properties of the molecular (Falgarone et al. 1991; Bensch et al. 2001, and references therein) and dust emissions (Gautier et al. 1992) in several regions. For HI, the power spectrum of the 21 cm emission has only been characterized in external galaxies (Stanimirovic et al. 1999; Elmegreen et al. 2001; Stanimirovic & Lazarian 2001) and in the Galactic plane (Crovisier & Dickey 1983; Green 1993; Dickey et al. 2001). These galactic studies were not centered on any particular

Send offprint requests to: M.-A. Miville-Deschênes,
e-mail: mamd@ias.u-psud.fr

Article published by EDP Sciences and available at http://www.aanda.org or http://dx.doi.org/10.1051/0004-6361:20031297

HI feature. Their analysis covered a depth in velocity which sampled more than one spiral arm, leaving the necessity of studying isolated features. Furthermore, the statistical properties of the column density do not allow one to fully characterize interstellar turbulence. For incompressible turbulent flows it is the velocity fluctuation power spectrum that follows a power law. Density fluctuations will appear self-similar in response to the velocity field, in certain conditions of compressibility or if the observed tracer is a passive scalar. Therefore, to study interstellar turbulence, it is important to deduce the statistical properties of both the velocity and density fields.

Centroid velocity fields have been used to study the kinematics of HII regions (Joncas & Roy 1986; O'Dell 1986; Miville-Deschênes et al. 1995; Godbout et al. 1997) and to describe the velocity structure of star forming regions (see Miesch et al. 1999 and references therein) in which it is believed that the velocity field may be strongly coupled to the density field and could have a direct impact on the star forming process and the initial mass function (Scalo & Chappell 1999). For the HI gas, studies have addressed only external galaxies (Spicker & Feitzinger 1988; Stanimirovic & Lazarian 2001) with no observational study to determine the 3D statistical properties of Galactic interstellar velocity fields. Recently, using fractional Brownian motion simulations, Miville-Deschênes et al. (2003) showed that the power spectrum of the 3D velocity field of optically thin media can be determined directly from the centroid velocity field.

In this paper, we propose an analysis of interferometric 21 cm observations of the Ursa Major Galactic cirrus. The vast majority of the Galactic cirrus (named for their resemblance to terrestrial cirrus in the IRAS all sky maps, Low et al. 1984) are composed of neutral hydrogen (HI and H_2) and dust; they represent the most abundant state (by mass) of interstellar matter in the Galaxy. We have selected this nearby high latitude cloud for our statistical analysis to minimize the importance of velocity crowding and to study the small-scale structure of the HI. We have also chosen a cloud for which the inertial range of interstellar turbulence (Tennekes & Lumley 1972) could be studied, meaning far from scales where energy inputs and dissipation occur (the viscous dissipation scale is thought to be ~10 AU in the HI – Falgarone & Puget 1995). The Ursa Major cirrus does not show any star formation activity (Magnani et al. 1990) and it is located at the edge of an expanding shell: the North Celestial Loop (Heiles 1989; Meyerdierks et al. 1991). Therefore, it is reasonable to assume that the main mechanical energy input comes from the expanding shell, at scales much larger (≥30 pc) than the field observed (~5 pc). The absence of stellar winds or outflows prevents the presence of energy injection at intermediate scales. Finally, the observed cloud is optically thin at 21 cm which is a required condition to deduce the statistical properties of the 3D density and velocity fields from projected quantities (Miville-Deschênes et al. 2003).

The first three sections of the paper present the observations (Sect. 2), the processing used to enhance the signal-to-noise ratio of the data (Sect. 3) and the 21 channel maps (Sect. 4). Then we present a power spectrum analysis of the integrated emission map, the centroid velocity field and of individual channel maps (Sect. 5). This analysis allowed us to determine the spectral index[1] of the 3D density and velocity fields of the HI gas. Our results are discussed in Sect. 6.

Table 1. Log of the DRAO observations. When the two fields are mosaiced together, this data set contains a total of 107 482 spectra.

Parameter	Value
Field 1	α_{2000} = 9h47m
	$\delta_{2000} = 70°30'$
Field 2	α_{2000} = 9h28m
	$\delta_{2000} = 70°10'$
Channel separation	0.412 km s^{-1}
Channel resolution	0.66 km s^{-1}
Number of channels	128
$V_{\rm min}$	−6.6 km s^{-1}
$V_{\rm max}$	19.4 km s^{-1}
Angular resolution	$0.99' \times 1.06'$
Field of view of each field	2.6°

2. Observations

The data were obtained using the Synthesis Radio Telescope of the Dominion Radio Astrophysical Observatory (DRAO) (Landecker et al. 2000). Two fields were observed and mosaiced; one in 1989 (Joncas et al. 1992) and the second one in 1995. The observational parameters of both fields are reproduced in Table 1. The only difference between the two epochs was the addition of three new antennas to the interferometer. In both cases the calibrators were 3C147 and 3C309.1 (Baars et al. 1977). DRAO is also equipped with a 26 m single dish telescope; HI observations taken with this dish are calibrated using S7 ($T_{\rm b}$ = 100 K). The combination of the observations made by both telescopes (synthesis and single dish) allows the complete coverage of the u-v plane down to the smallest scale resolved by the synthesis telescope (see Taylor et al. 2003 where the combination procedure is extensively described).

The mean 21 cm spectrum of the Ursa Major cirrus, taken with a beam of 30 arcmin with the Leiden/Dwingeloo telescope (Burton & Hartmann 1994), is shown in Fig. 1. The main HI component is near 5 km s^{-1} but there is also an intermediate velocity component near −55 km s^{-1}, possibly related to the Perseus arm. In order to study the kinematics of the gas we have selected a channel width of 0.41 km s^{-1}. The real velocity resolution is 0.65 km s^{-1} due to filter spillover. Considering the number of channels of the spectrometer (see Table 1) we have limited our observations to the main HI component (see Fig. 1). This compromise between spectral resolution and velocity span allows us to scan more than 80% of the emission with a velocity resolution good enough to resolve the thermal broadening of the CNM.

[1] We refer to the spectral index as the exponent of the power spectrum assuming it can be represented by a power law.

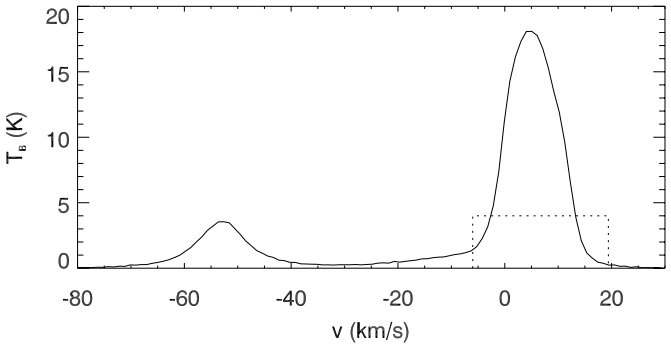

Fig. 1. Low resolution average spectrum (from the Leiden/Dwingeloo survey) of the Ursa Major cirrus observed with DRAO. The spectral range covered at DRAO is delineated by a dotted line.

3. Data processing

The preliminary steps of the reduction were done at DRAO (combination of the observations from the interferometer and from the single dish, construction of the channel maps). These standard operations are described in Joncas et al. (1992). The observations presented in this paper are characterized by a somewhat low signal-to-noise ratio ($\lesssim$15 – see Fig. 4). This is partly compensated for in the statistical studies we present here by the large size of the sample. Once mosaiced together, the data set contains 107 482 spectra[2]. In this section we present the filtering method we have used to increase the signal-to-noise ratio of the data.

3.1. Characterization of the noise

The observations have been conducted such that there are some channels with basically no HI emission. These channels are used to characterize the noise. An empty channel of the combined Ursa Major observations (see Fig. 2 – middle) shows that the noise level is not spatially uniform. In the combination of the interferometric and single dish observations we have normalized the data for the beam of the single dish. This operation increases the noise level near the edge of the field. This increase is quantified by computing the standard deviation of the high frequency fluctuations (high-pass filtering) on each spectrum of the data cube (see Fig. 2 – bottom). The noise level varies from ~3 to ~13 K from the center to the edge of the field. Figure 2 – top shows the power spectrum[3] of a sub-region of an empty channel (see white rectangle in Fig. 2 – middle). There is an increase of power at large scales ($k < 0.02$ pixel^{-1}) mainly due to the increase of the noise level on the side of the field. Part of this increase could also be attributed to the lower statistics of the large scale, an effect inherent to finite size images. At small scales ($k > 0.3$ pixel^{-1}) the abrupt power drop is due to the beam of the interferometer. But in the intermediate regime the power spectrum is relatively flat which is an indication of the uniformity of the u-v plane coverage.

[2] As the angular resolution is ~1′×1′ and the pixel size is 0.5′×0.5′, the number of independent spectra is 1/4 of that value (~26 870).

[3] The technique used to compute the power spectrum is described in Sect. 5.2.

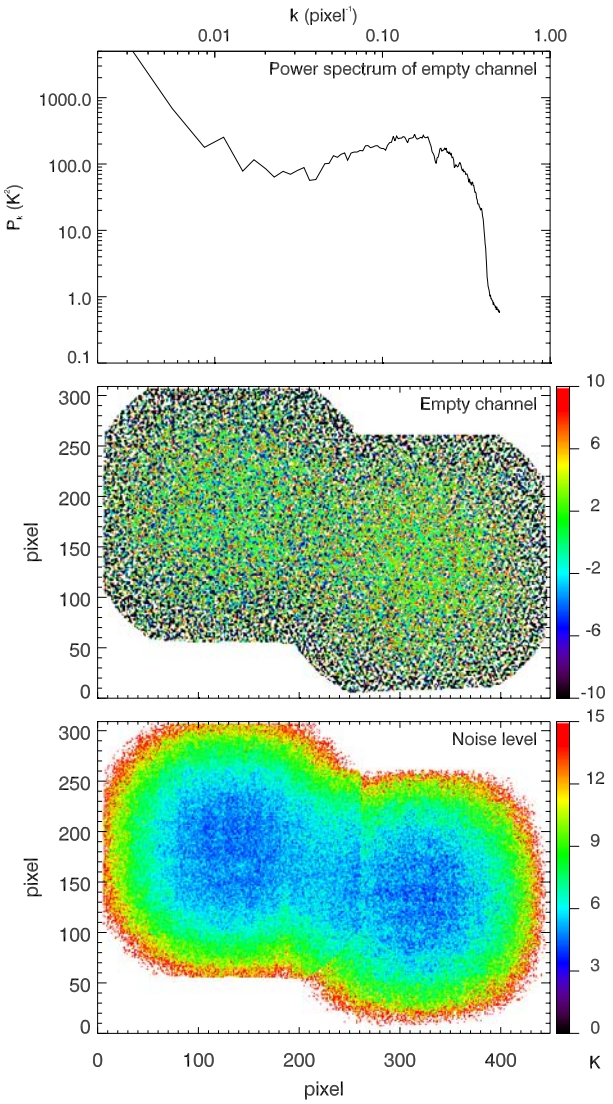

Fig. 2. Middle: empty channel of the combined Ursa Major observations. Top: power spectrum of a sub-region of the empty channel (white rectangle in Middle panel). Bottom: noise level at each position, estimated by the standard deviation of each spectrum high frequency fluctuations.

3.2. Filtering

To increase the signal-to-noise ratio of this type of spectro-imaging data we have developed a method based on a wavelet decomposition of each channel. This method, an adaptation of the work of Starck & Murtagh (1998), looks for structures that are significant in terms of signal-to-noise ratio and that are also coherent in the spectral domain. To optimize the filtering we have used our knowledge of the spectral and spatial variations of the noise level.

First each channel $c_0(x, y, v)$ of the data cube was decomposed on a wavelet basis using the "a trou" algorithm:

$$c_0(x, y, v) = c_p(x, y, v) + \sum_{l=1}^{p} w_l(x, y, v), \quad (1)$$

where the $w_l(x, y, v)$ are the wavelet coefficients at a given scale l and the $c_p(x, y, v)$ are the large scale residuals. Then,

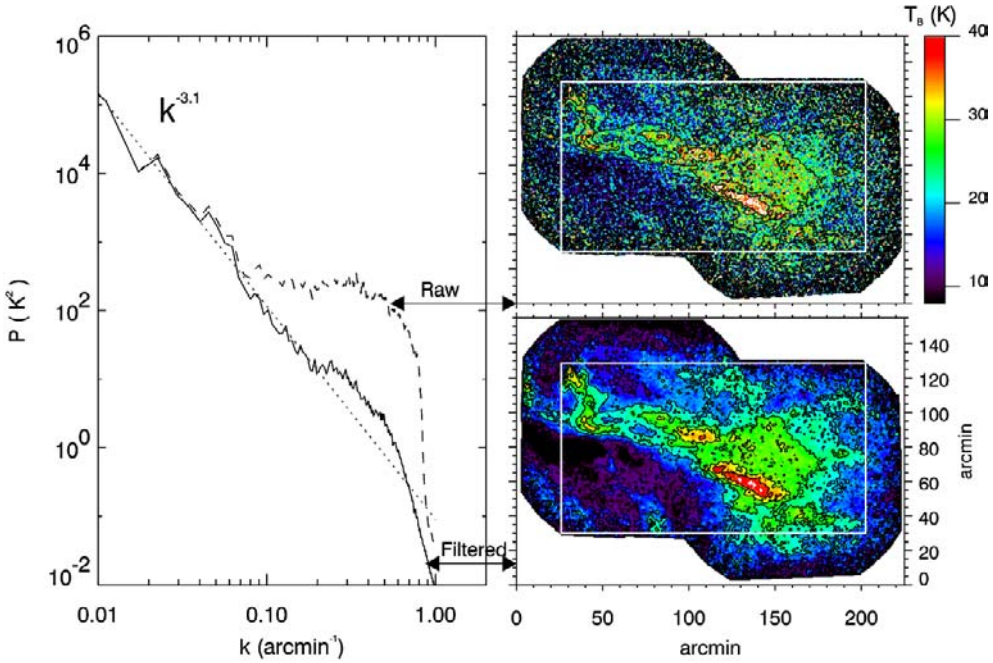

Fig. 3. Example of the filtering on an individual channel map. Top-right: raw data. Bottom-right: filtered data. Note the presence of a weak elongated structure in the south-eastern part of the field, running from (50′, 80′) to (90′, 40′), barely visible in the raw data and preserved by the filtering method. Left: power spectrum of the channel map (inside the white rectangle area), before and after filtering. The pixel size is $30'' \times 30''$.

the wavelet coefficients $w_l(x, y, v)$ are compared to the amplitude of the noise $n_l(x, y)$ at each scale and position. The $n_l(x, y)$ were computed as

$$n_l(x, y) = A_n(x, y) \times \sigma_n(l) \quad (2)$$

where $A_n(x, y)$ is the noise level as a function of position (Fig. 2 – bottom) and $\sigma_n(l)$ is the dispersion of the wavelet coefficients of a white noise image with a standard deviation of one (Starck & Murtagh 1998).

If the wavelet coefficient satisfies the following criterion:

$$|w_l(x, y, v)| > 1.5 \times n_l(x, y) \quad (3)$$

it is kept, otherwise it is put to zero. Each channel is then reconstructed with the significant wavelet coefficients using Eq. (1). Starck & Murtagh (1998) suggest a threshold of 3 but we have chosen to be more conservative using a threshold of 1.5 to limit the removal of real weak and extended structures from the data.

This filtering removes all the fluctuations that do not have a significant signal-to-noise ratio, but there are always strong noise peaks that are not removed. To detect these noise peaks, we use the fact that they are not correlated from one channel to the other. In practice, each spectrum is checked for discontinuities larger than 8 K that go up and down (or down and up) in one or two channels. These noise peaks were removed and the missing values were interpolated on the spectral axis.

An example of the filtering on a channel map is shown in Fig. 3. The power spectrum of this channel map, computed before and after filtering (see Fig. 3) shows that the noise in the raw data dominates the signal at scales smaller than ∼20′. With the filtering technique applied here, we were able to lower the noise significantly, decreasing the scale range dominated by noise. In the filtered channel map shown here, the noise becomes important at scales smaller than ∼4′ (8 pixels).

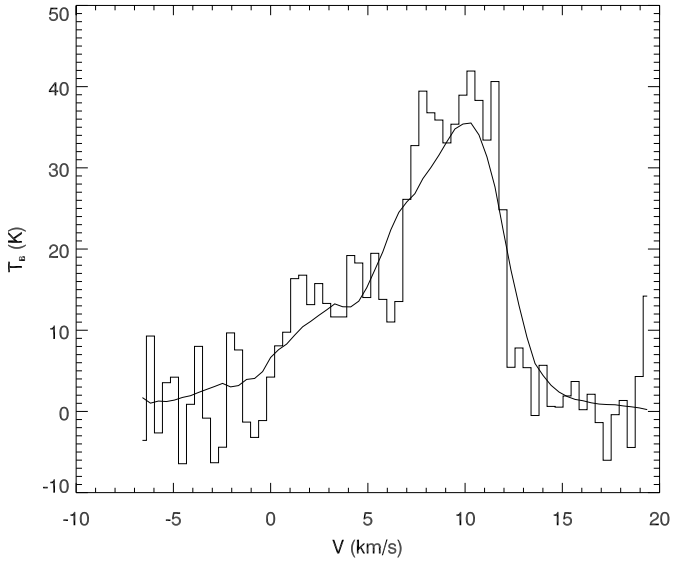

Fig. 4. Typical 21 cm spectrum of the DRAO observation, before (histogram) and after (continuous line) the filtering.

The filtering applied to the data allows the detection of spatially coherent structures that had a signal-to-noise ratio down to 1 in the raw channel maps. For instance, in Fig. 3 we note the presence of a weak elongated structure in the south-eastern part of the field, running from (50′, 80′) to (90′, 40′), that was barely visible in the raw data. This very thin filament has a thickness of ∼0.06 pc and a length of greater than 1 pc. The filtering has also reduced considerably the noise in individual

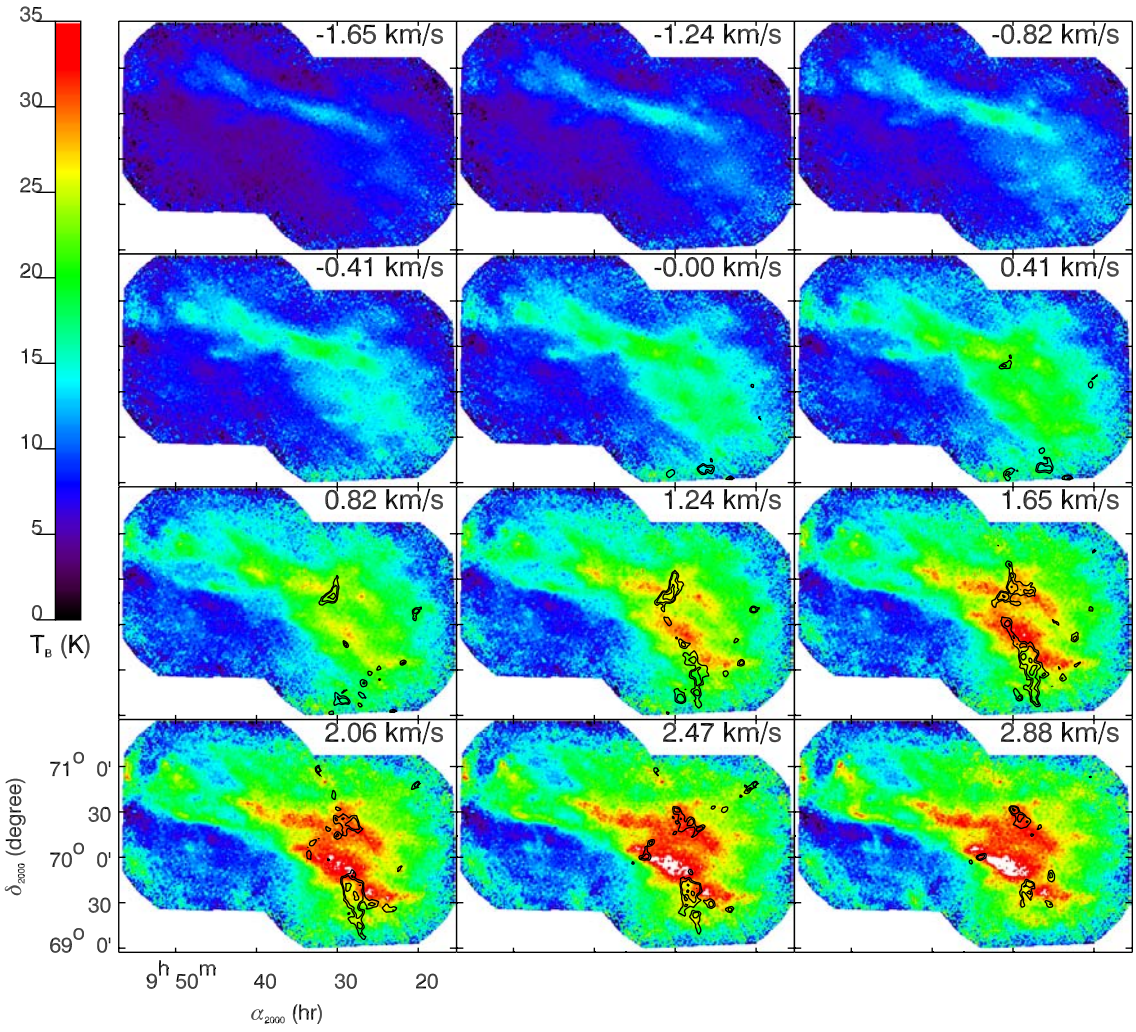

Fig. 5. Ursa Major. Channel maps of the 21 cm line emission between −1.65 and 2.88 km s^{-1}. The contours (1.5, 2 and 3 K) represent the CO emission of Pound & Goodman (1997).

spectra as shown in Fig. 4. This is of major importance for the analysis of the velocity field.

4. The 21 cm data of the Ursa Major cirrus

4.1. 21 cm channel maps

The Ursa Major cirrus is composed of two connected parts. The eastern region (field 1) is predominantly atomic as it is detected only in the HI line. The western region (field 2) presents significant CO emission (Pound & Goodman 1997). The data from field 1 has already been discussed by Joncas et al. (1992) but the data processing techniques used since then have given a second life to these data. Figures 5 to 7 show the HI mosaic in a series of panels separated by 0.412 km s^{-1}. The velocity is indicated in the upper right portion of each panel. The brightness temperature in the channel maps varies from 1 K to 40 K. The CO emission as observed by Pound & Goodman (1997) is present from 0.0 km s^{-1} to 3.71 km s^{-1}. It is shown in contours, superimposed on the HI emission, in Figs. 5 to 7.

The 21 cm channel maps show an intricate structure of interwoven elongated structures with aspect ratio up to 15. For the sake of simplicity, we call them filaments in the following, but, as indicated by Lazarian & Pogosyan (2000), we are aware that the structure identified in any channel map reflects more velocity features than density enhancements. Therefore we deliberately restrain the description of the structure observed in channel maps. Nevertheless it is interesting to point out that the western region, where CO emission is observed, shows generally less filamentary structure than the eastern part of the field where no molecular emission is detected. The detailed comparison of the molecular and atomic components of the cloud, which is clearly beyond the scope of this paper, is important to understand the specific dynamical conditions that lead to the formation of long-lived molecular clouds. We leave this to a further study.

4.2. Integrated emission map

One important quantity that can be derived from 21 cm data cubes is the integrated emission which, for optically thin media, is related to the column density of HI. The 21 cm brightness

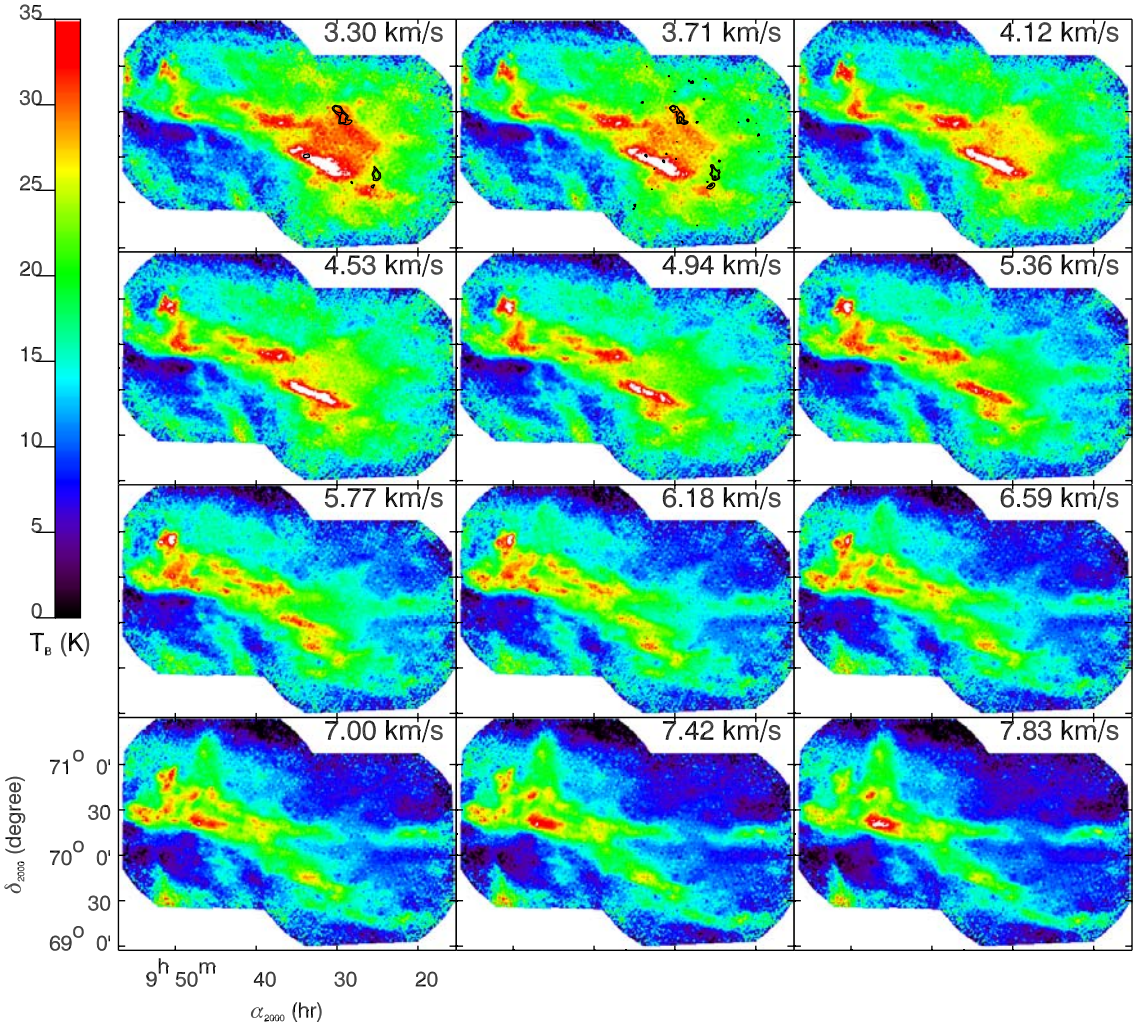

Fig. 6. Ursa Major. Channel maps of the 21 cm line emission between 3.30 and 7.83 km s^{-1}. The contours (1.5, 2 and 3 K) represent the CO emission of Pound & Goodman (1997).

temperature $T_{\rm B}(v)$ at a given velocity v and within δv of HI gas having a kinetic temperature $T_{\rm k}$ is given by:

$$T_{\rm B}(v) = T_{\rm k}\,(1 - \exp\,(-\tau(v))) \tag{4}$$

where

$$\tau(v) = \frac{N(v)}{C \times T_{\rm k} \delta v}, \tag{5}$$

$N(v)$ being the gas column density at velocity v and within δv, and $C = 1.823 \times 10^{18}$ cm^{-2} K^{-1} km^{-1} s (Kulkarni & Heiles 1987). In the optically thin regime ($\tau(v) < 1$), the column density can be estimated without knowing the kinetic temperature of the gas. In the optically thin approximation

$$N(v) = C \times T_{\rm B}(v) \delta v. \tag{6}$$

As shown in Fig. 8, the effect of opacity on the determination of the column density is stronger for cold gas and for high brightness temperatures. For warm HI ($T_{\rm k} > 500$ K), the opacity is negligible and the column density is well approximated by Eq. (6). On the other hand, for a typical CNM kinetic temperature (∼100 K) and a brightness temperature of ∼40 K (the maximum value in our channel maps), the column density in a given channel map is underestimated by ∼20%. But the 21 cm profiles are relatively broad and most of the brightness temperature values are below 20 K. Therefore, if the kinetic temperature of the HI in Ursa Major is ∼100 K, we think that the column density is probably underestimated by only ∼10% in the brightest region of the cloud, which confirms that we are in the optically thin regime.

Instrumental noise also affects the determination of the column density. Since the uncertainty on the column density increases with the square root of the number of independent channels used in the summation, it is common to define a spectral window within which the column density is computed. In this way, noise contribution from the empty channels is avoided. However for these observations the baseline is very short (see Fig. 4) and varies in length at both ends as a function of the Doppler shifts of the line emission. Therefore all channels were summed.

The integrated emission map of the Ursa Major field is shown in Fig. 9. This map is characterized by a set of filaments, mainly oriented west-east. The integrated emission peaks at $W \approx 330$ K km s^{-1} (corresponding to $N_H \sim 6 \times 10^{20}$ cm^{-2}) in the eastern part of the main filament. The mean

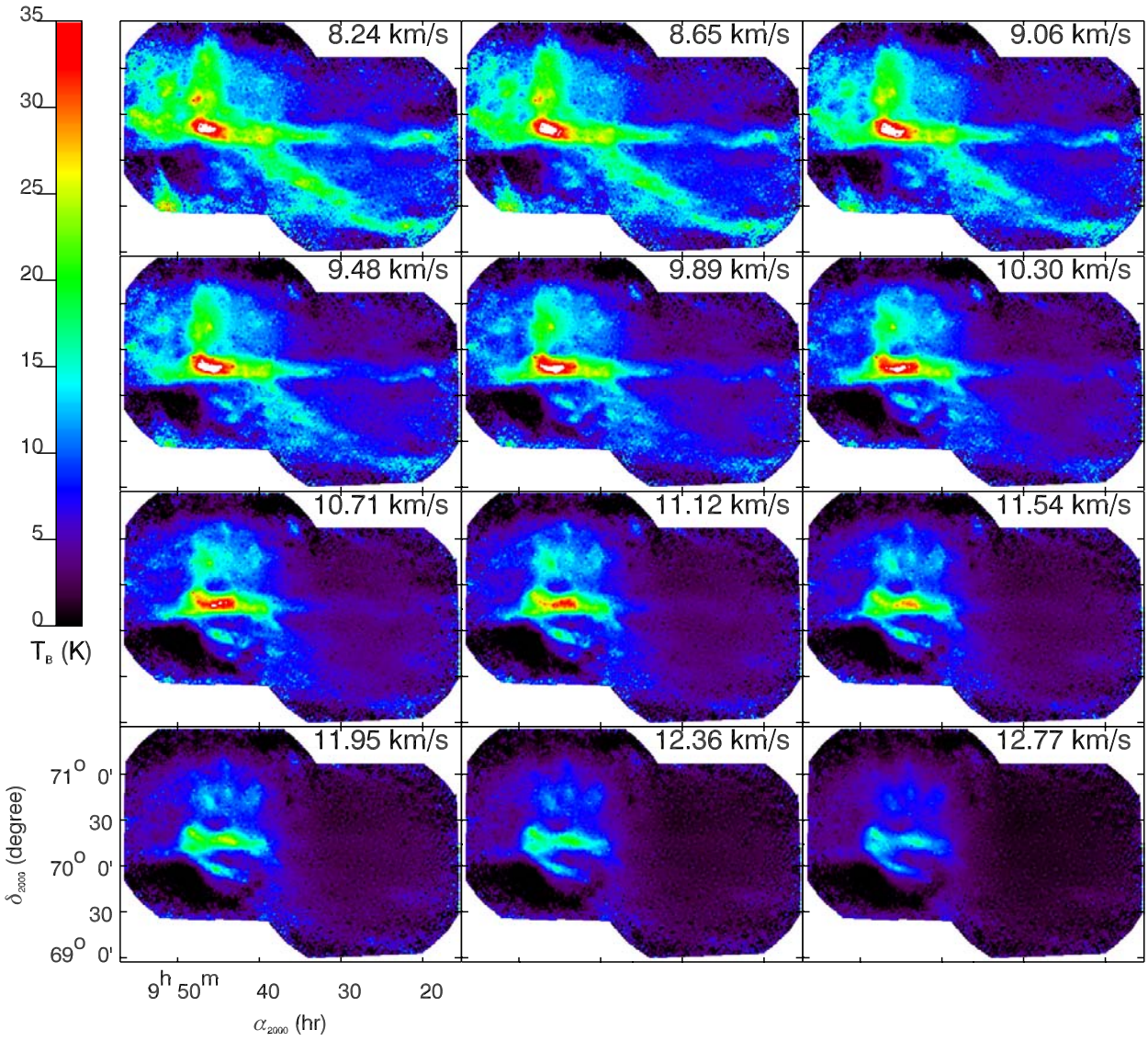

Fig. 7. Ursa Major. Channel maps of the 21 cm line emission between 8.24 and 12.77 km s^{-1}.

integrated emission value in the field is $W \approx 190$ K km s^{-1} ($N_H \sim 3.45 \times 10^{20}$ cm^{-2}).

4.3. Centroid velocity field

The centroid velocity field $C(\alpha, \delta)$ of a position-position-velocity (PPV) data cube $T_{\rm B}(\alpha, \delta, v)$ is given by the following expression:

$$C(\alpha, \delta) = \frac{\sum_v v \times T_{\rm B}(\alpha, \delta, v)}{\sum_v T_{\rm B}(\alpha, \delta, v)} \ {\rm km\,s^{-1}}. \quad (7)$$

For optically thin clouds, the centroid velocity field is exactly the mean radial velocity of the gas on the line of sight. As shown by Pety (1999), noise significantly affects the determination of velocity centroids. In fact, the error on the velocity centroid determination depends on the signal-to-noise ratio of the spectrum and on the number of channels used. To minimize the effect of noise, one may compute the centroid velocity on each spectrum by selecting a spectral window on each spectrum where all the brightness temperatures are greater than twice the noise level. But practically, the wavelet filtering we have applied significantly reduces the noise level of the data leaving very few noise peaks that could contaminate the centroid velocity estimate. Therefore, and as there are very few channels with no emission, all the channels were used to compute the centroid velocity of each spectra. The centroid velocity field of the Ursa Major cirrus is shown in Fig. 10.

The centroid velocity field of the Ursa Major cirrus is characterized by a set of elongated structures. The two main elongated structures seen in the integrated emission map and in channel maps also stand out in the centroid velocity field. Velocity fluctuations are observed at all scales, up to the largest one where there is an east-west velocity gradient of ~1.5 km s^{-1} pc^{-1} at a 2° scale (considering a distance of 100 pc for the cirrus). But it is at small scales that the velocity gradients are the largest. Across the brightest filament of the cirrus (near position (50′, 80′) in Fig. 10) we observe

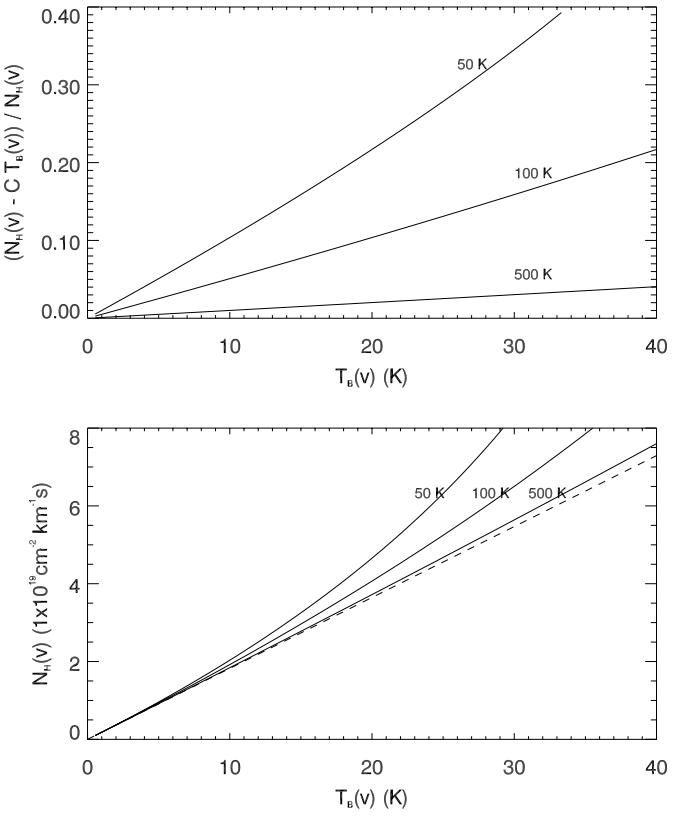

Fig. 8. Error on the column density estimate using the optically thin approximation (Eq. (6)) for HI gas with a kinetic temperature of 50, 100 and 500 K. Bottom: the column density (per velocity interval) determined using the optically thin approximation as a function of brightness temperature is given by the dashed line. The three continuous lines indicate the real column density (per velocity interval) of the gas as a function of brightness temperature. Top: fraction of the real column density that is missed in the optically thin approximation as a function of the brightness temperature at a given velocity.

transverse velocity gradients between ∼5 and 10 km s^{-1} pc^{-1}, at a 20′ scale (also shown by Miville-Deschênes et al. 2002).

5. Power spectrum analysis

5.1. Determination of the density and velocity power spectra in three dimensions

One important aspect of the study of interstellar turbulence is to determine the statistical properties of the density and velocity fields in three dimensions (3D). To do so one must understand the effect of opacity and of projection on the observed quantities. Regarding density fluctuations, many authors (Stutzki et al. 1998; Lazarian & Pogosyan 2000; Goldman 2000; Miville-Deschênes et al. 2003) have shown that the power spectrum of the 3D density field can be determined directly from the power spectrum of the integrated emission map under two conditions: 1) the observed medium must be optically thin and 2) the spatial scales observed on the plane of the sky must be smaller or equal to the spatial depth of the line of sight. Under these conditions, the power spectrum of the integrated emission map is proportional[4] to the power spectrum of the 3D density field.

The determination of the 3D velocity field power spectrum is less obvious. Lazarian & Pogosyan (2000) proposed a method called Velocity Channel Analysis (VCA) that uses the variation of the spectral index of velocity slices of increasing thickness. But as pointed out by Miville-Deschênes et al. (2003) and as we will show here, this method is very difficult to apply to real observations. On the other hand, Miville-Deschênes et al. (2003) showed that centroid velocity fields can be used to determine the power spectrum of the 3D velocity field. Using Fractional Brownian Motion simulations[5] these authors studied the impact of density and velocity fluctuations on the power spectrum of centroid velocity fields. They showed that density fluctuations have a very limited effect and that the power spectrum of the centroid velocity field is the same as for the 3D velocity field, assuming that the medium observed is optically thin and that the scales observed on the sky are smaller than the depth of the line of sight.

It is important to estimate if these results can be applied to the specific physical conditions of the Ursa Major cirrus. First, we have shown that opacity effects are limited for the brightness temperature observed here (see Fig. 8). Second, as the cloud is at 100 pc, the largest transverse scale in the field is only ∼7 pc, which is very likely to be smaller than the depth of the HI froth in that region (probably several tens of pc if we look at large scale observations – see Fig. 12). Therefore, in the following we analyze the power spectrum of the integrated emission map and of the centroid velocity field of the Ursa Major cirrus in the framework of Miville-Deschênes et al. (2003).

5.2. Integrated emission map and centroid velocity field

For the Ursa Major observations, we have limited the power spectrum computation to a rectangular region (354 × 198 pixels) where all the points have been observed. This sub-region is delimited by a white rectangle in Figs. 3, 9 and 10. The power spectrum is the sum of the square of the real and imaginary parts of the two dimensional FFT, azimuthally averaged over each wavenumber $k = \sqrt{k_x^2 + k_y^2}$. As stated by Bensch et al. (2001), edge effects may introduce systematic bias in the determination of the power spectrum index using Fast Fourier Transform algorithms. When the power spectrum is described by a power law $P(k) \propto k^\beta$, the error on the power spectrum index depends on β itself; it becomes important for $\beta < -3$. To reduce this effect, we have apodised the edge of the image with a cosine function. The size of the apodised region is equal to 3% of the linear size of the image. We have tested this method on non-periodic Fractional Brownian Motion images (Miville-Deschênes et al. 2003) and we have found that the β value is recovered with a typical error of 0.1 for $-4 < \beta < -2$.

[4] It has the same shape – or spectral index – but not the same normalisation.

[5] Fractional Brownian motion simulations produce self-similar Gaussian random images.

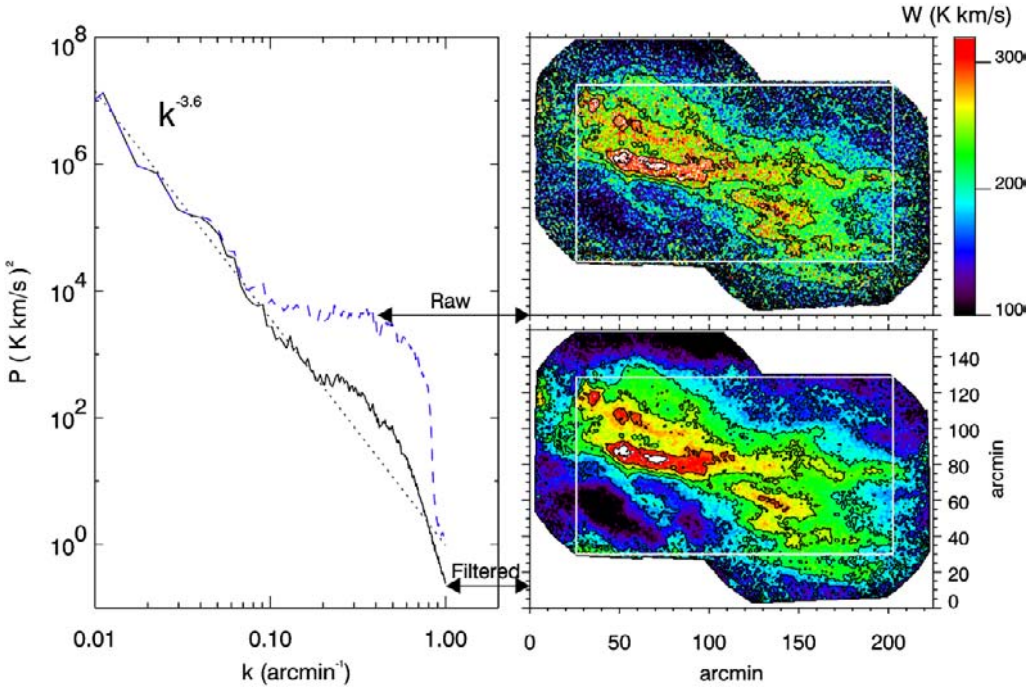

Fig. 9. HI Integrated emission of the Ursa Major cirrus Right-top: raw data. Right-bottom: filtered data. Left: power spectrum of the integrated emission map of the raw and filtered data. The dotted line represents a power law with a spectral index of −3.6.

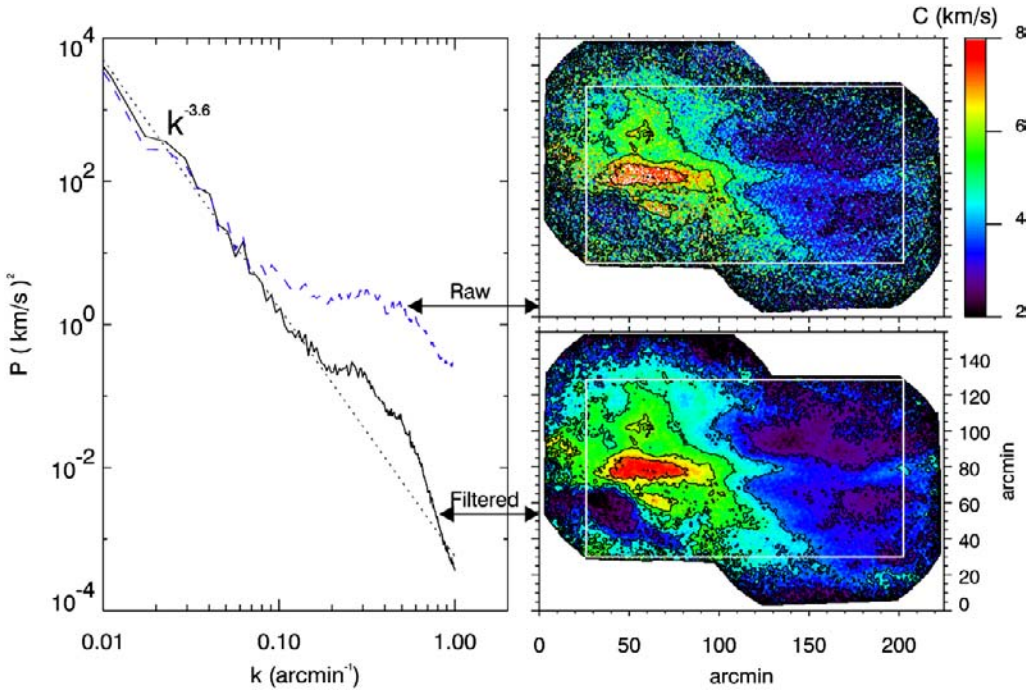

Fig. 10. HI centroid velocity field of the Ursa Major cirrus Right-top: raw data. Right-bottom: filtered data. Left: power spectrum of the centroid velocity field of the raw and filtered data. The dotted line represents a power law with a spectral index of −3.6.

The power spectra (raw and filtered data) of the integrated emission map and centroid velocity field are shown in Figs. 9 and 10. For both the integrated emission map and the centroid velocity field the power spectrum of the filtered data is well described by a power law $\propto k^{-3.6\pm0.2}$ for wavenumbers $0.01 < k < 0.2$ arcmin^{-1}. We have to restrict the slope determination to a relatively narrow scale range for two reasons. First, at large scale, the 1D power spectrum points have a large uncertainty as they are the average of a small number of samples in the 2D FFT. Second, at small scales, the power spectrum is affected by the beam, the noise and the non-periodicity of the image mentioned earlier. The uncertainty on the spectral index we give in this paper (±0.2) reflects the dispersion of the P_k values around the power law but mainly the uncertainty related to

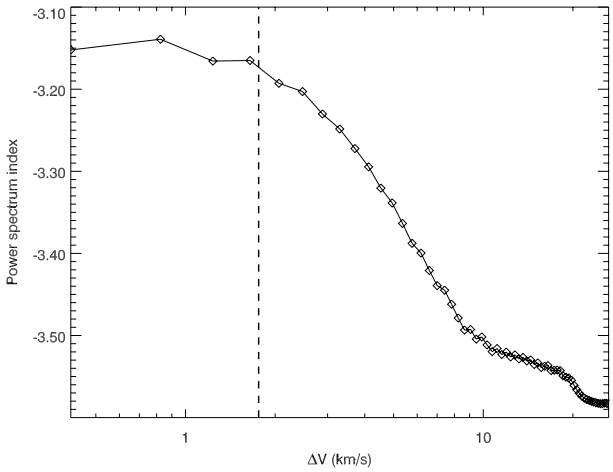

Fig. 11. Power spectrum index of velocity slices as a function of the slice width ΔV. Velocity slices are built by adding velocity channel maps from the the brightest to the faintest.

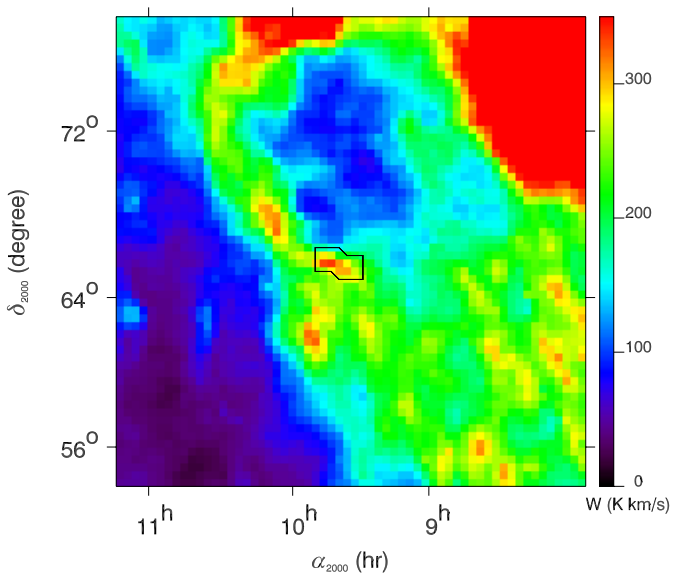

Fig. 12. Integrated emission of the 21 cm Leiden/Dwingeloo survey in the direction of the North Celestial Loop. The Ursa Major fields observed with the DRAO interferometer are indicated by boxes.

the apodization, beam and noise (see above). This uncertainty value has been validated using the fractional Brownian motion simulations and realistic noise and beam shape.

As opacity effects are negligeable at 21 cm and the depth of the cirrus is most probably larger than the largest transverse scale, we estimate that the 3D density and velocity fields of the Ursa Major cirrus are characterized by a spectral index $\gamma_v = \gamma_n = -3.6 \pm 0.2$. Here we consider that the energy driving the turbulent motions is injected at much larger scales than the size of the observed fields and that the behavior of the velocity field at all scales is inherent to the turbulent cascade. It is interesting to point out that the velocity spectral index is compatible with the value expected ($-11/3$) for Kolmogorov turbulence (Kolmogorov 1941).

5.3. Velocity channel analysis

As discussed earlier, Lazarian & Pogosyan (2000) proposed a method to determine the spectral index of the 3D density and velocity fields using PPV data cubes of optically thin media. This method has been used by a few authors to determine the 3D velocity spectral index γ_v of HI in the Galactic plane (Dickey et al. 2001) or in other galaxies (Stanimirovic et al. 1999; Stanimirovic & Lazarian 2001; Elmegreen et al. 2001). The VCA method is based on the analysis of velocity slices of increasing width ΔV. Lazarian & Pogosyan (2000) claim that the spectral index of velocity slices should reach two asymptotic states at small and large ΔV, from which γ_v could be determined.

We have tested the VCA method on our observations. Figure 11 shows the variation of the spectral index of velocity slices of increasing width ΔV. Here a velocity slice of width ΔV is the sum of the $N = \Delta V/\delta u$ brightest consecutive channel maps, where $\delta u = 0.412$ km s^{-1}. The spectral index of each velocity slice was computed; it is the slope of the power spectrum between $0.01 < k < 0.1$ arcmin^{-1}. As expected, at large ΔV the curve in Fig. 11 converges to the spectral index of the integrated emission (~ -3.6). At the other end, the curve reaches another asymptotic state to the value (~ -3.1) found for the brightnest channel map (see Fig. 3).

But here it is important to estimate the effect of the gas temperature on this curve. The vertical dashed line in Fig. 11 shows the effective spectral resolution of our observations $\delta v_{\rm eff} \approx \sqrt{\delta u^2 + 2.16 k_{\rm B} T/m} = 1.7$ km s^{-1} (where m is the mean atomic mass and if we consider typical CNM gas at $T = 150$ K – see Miville-Deschênes et al. 2003 for details). The plateau seen at small ΔV in Fig. 11 is simply the result of the gas temperature that washed out all velocity fluctuations in channel maps. Therefore, the asymptotic state at small ΔV is not the one expected by Lazarian & Pogosyan (2000) and cannot be used to determine γ_v. Like Miville-Deschênes et al. (2003) we conclude that while it could be used for large scale observations (i.e. external galaxies), the VCA technique is not suited to determine the 3D velocity spectral index for local HI where the velocity dispersion is commensurate with the thermal broadening on a broad range of scales.

5.4. Combination with Leiden observations

To obtain a more global view of the HI power spectra (integrated emission and centroid velocity) we combined the power spectra computed on the Ursa Major DRAO observations with the power spectra computed on the Leiden/Dwingeloo observations of the whole North Celestial Loop region (which includes the Ursa Major cirrus) as observed by the Leiden/Dwingeloo survey (see Figs. 12 and 13). The angular scales of each observation complement very well to give the power spectrum of the HI integrated emission and of the centroid velocity fields over almost three orders of magnitudes in scales, from 2 arcmin to 16 degrees (see Figs. 14 and 15). One outstanding result of this analysis is the fact that both power spectra are compatible with a single slope of -3.6 ± 0.2 over the whole range of scales. The decrease of power at small scales ($k > 0.4$ arcmin^{-1}) is due

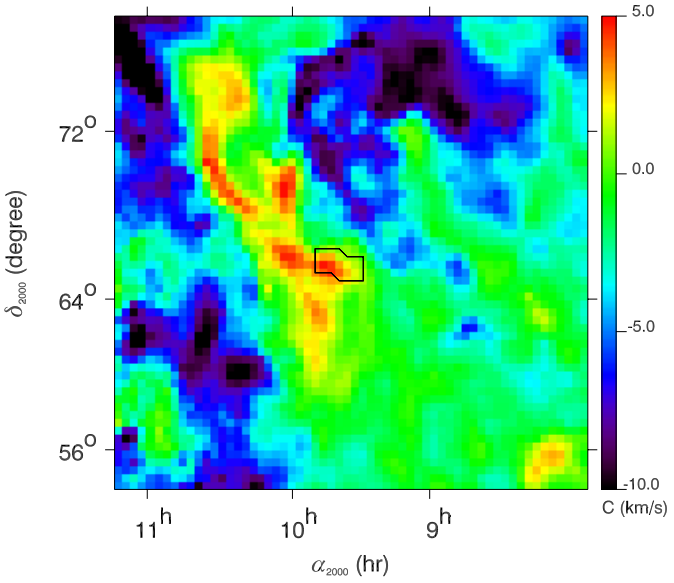

Fig. 13. Centroid velocity field of North Celestial Loop (Leiden/Dwingeloo data). See Fig. 12.

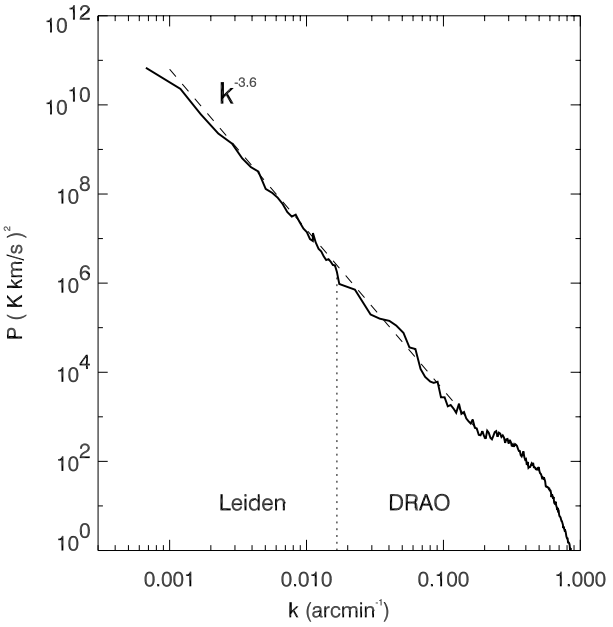

Fig. 14. Power spectrum of the integrated emission of the Ursa Major / North Celestial Loop region. The dotted line defines the scale regimes of the DRAO and Leiden/Dwingeloo data (see Fig. 12). The dashed line represents a slope of −3.6.

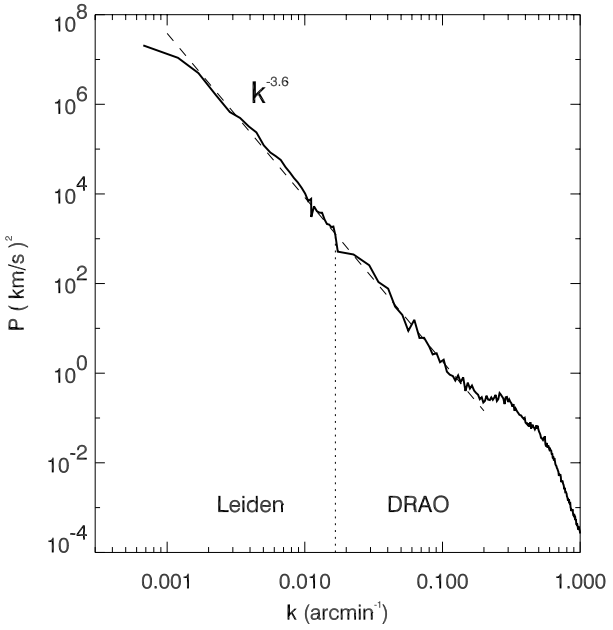

Fig. 15. Power spectrum of the centroid velocity field of the Ursa Major / North Celestial Loop region. The dotted line defines the scale regimes of the DRAO and Leiden/Dwingeloo data (see Fig. 13). The dashed line represents a slope of −3.6.

to the domination of the noise at these scales. All the power at these scales was removed by the wavelet filtering. At the other end of the power spectrum, the flattening may not be significant as the statistics at large scale are low. If we consider that most of the gas in the North Celestial Loop is local, at an approximate distance of 100 pc (Penprase 1993), and the opacity effects are limited in the region, the local HI is self-similar on spatial scales from 0.5 to 25 pc.

5.5. Density-velocity correlation

The structure of the centroid velocity field of the DRAO fields shows many similarities to the column density map. In both maps, the main filaments of the cirrus are visible, indicating that the density and velocity of the HI show some correlation. This is also true at larger scales as one can see in Figs. 12 and 13 where we show the integrated emission and the centroid velocity field of the North Celestial Loop (Leiden/Dwingeloo data). At the scale of the loop, the main density structures seen in the integrated emission map are correlated with structure in the centroid velocity field.

To estimate the correlation level between the column density and the velocity field, we have computed the cross-correlation defined as:

$$Ccr = \frac{\langle N_{H\mathrm{tot}}\, V_c\rangle - \langle N_{H\mathrm{tot}}\rangle \langle V_c\rangle}{\sigma_N \sigma_V} \quad (8)$$

where σ_N and σ_V are the standard deviation of the column density and centroid velocity fields respectively. The cross-correlation is 0.44 for the Ursa Major field and 0.25 for the North Celestial Loop region, indicating a moderate correlation between the centroid velocity and column density field.

6. Discussion

As shown by Lazarian & Pogosyan (2000) and Miville-Deschênes et al. (2003), the interpretation of the power spectrum of individual channel maps is not unique since brightness fluctuations in a channel map are the combination of velocity, density and temperature fluctuations. On the other hand, for optically thin and isolated regions, and at scales that are smaller than the depth of the observed region, the power spectrum of the HI integrated emission is exactly the power spectrum of the 3D density field. Furthermore,

under these conditions and in the case of Gaussian fields, Miville-Deschênes et al. (2003) show that the power spectrum of the centroid velocity field is exactly the power spectrum of the 3D velocity field.

With these ideas in mind, it is interesting to compare our results ($\gamma_n = -3.6 \pm 0.2$ and $\gamma_v = -3.6 \pm 0.2$) with previous power spectrum analysis of 21 cm observations, and try to draw a coherent picture of the HI density and velocity statistical properties. First, Crovisier & Dickey (1983), Green (1993), Deshpande et al. (2000), Dickey et al. (2001) all found a spectral index of $\sim -2.9 \pm 0.2$ for individual channel maps of Galactic plane regions with significant emission, in accordance with our values for individual channels in the line center (see Figs. 3 and 11). But, as it has been said before, the contribution of the velocity, density and temperature fluctuations to the structure in individual channel maps makes these spectral indexes very difficult to interpret. Aware of this, Dickey et al. (2001) also looked at the spectral index of the integrated emission which, in their most out-of-plane region ($b = 1.3°$), is ~ -4. However, one must keep in mind that the power spectrum of an integrated emission map of Galactic plane regions could be affected by non-turbulent large scale structure and by significant HI self-absorption. Recent high-resolution ($1'$) 21 cm observations (Gibson et al. 2000) have shown the presence of several HI self-absorption regions in the Galactic plane, that could not be detected in previous low-resolution 21 cm surveys. As self-absorption seems to be more important at small-scale, it could reduce significantly the amplitude of the small-scale HI emission and produce an artificial steepening of the power spectrum. Lets also mention the work of Deshpande et al. (2000) who looked at the power spectrum of the velocity-integrated HI optical depth, using absorption measurements in the direction of Cassiopeia A. They found a relatively high spectral index (-2.75 ± 0.25) but, as they pointed out, the optical depth depends both on the column density and the gas temperature which makes the relation to the 3D density power spectrum not straightforward.

Recently there have also been some power spectrum analyses performed of 21 cm emission in external galaxies. For instance Stanimirovic & Lazarian (2001) found $\gamma_n = -3.3$ for the HI integrated emission in the Small Magellanic Cloud (scales from 30 pc to 4 kpc). In the Large Magellanic Cloud, Elmegreen et al. (2001) found that the power spectrum of the HI integrated emission is well described by two power laws of indexes −3.66 and −2.66, on spatial scales between 20 pc and 9 kpc. The spectral index change, which occurs near $L \sim 100$ pc, can be explained by the fact that the scales on the plane of the sky are larger than the depth of the medium for $L > 100$ pc. In this case, the steepening of the slope observed at small scales reflects a change in the topology of the medium investigated from a 2D (large scales) to a 3D (small scales) system, an effect described by Miville-Deschênes et al. (2003). The density spectral index measured by Elmegreen et al. (2001) in the LMC is in accordance with our γ_n value, even if their smallest scale corresponds approximately to our largest scale. On the other hand, contrary to Elmegreen et al. (2001) we do not observe a break in the slope of the power spectrum which indicates that the scale range we trace (from 0.1 to 25 pc) is smaller than the typical depth of the medium. This is in agreement with the fact that the scale height of Galactic HI is ∼100 pc (Lockman & Gehman 1991).

The diversity of HI spectral indexes found in the litterature reveals the importance of gas temperature, depth, energy injection and opacity effects on the power spectrum of 21 cm emission and how difficult it is to determine accurately the 3D statistical properties of interstellar turbulence. Unlike most of the HI studies done so far, 21 cm observations of high latitude regions like the one presented in this work offer the most favorable physical conditions to determine the 3D density and velocity power spectrum of interstellar turbulence. Such regions are almost unaffected by self-absorption and their density and velocity fields are dominated by turbulent motions, which is not always the case for Galactic plane regions and external galaxies where energy injection at several scales by supernovae, stellar winds or outflows might affect the power spectrum. The work we present in this paper is the first study of the inertial range of interstellar turbulence, far from energy injection and dissipation scales, and where opacity and projections effects are controled. It is the first time that the 3D density and velocity power spectra, essential quantities for the understanding of interstellar turbulence, are determined for the Galactic interstellar medium. Furthermore, the dynamical range of scales over which they are measured (more than two orders of magnitude) is larger than for all previous studies. The existence of these two scaling laws is therefore a robust result.

It is important to point out that our results ($\gamma_n = -3.6 \pm 0.2$ and $\gamma_v = -3.6 \pm 0.2$) agree with the Kolmogorov prediction for incompressible turbulence ($-11/3$). It may indicate that compressibility and magnetic field do not affect significantly the energy cascade of interstellar turbulence. Our results are in accordance with the work of Goldreich & Sridhar (1995) (see also the review of Cho et al. 2003) who predicts a Kolmogorov type energy spectrum for an incompressible turbulent magnetized fluid. But Goldreich & Sridhar (1995) also predict an anisotropy of the velocity and density fluctuations that increases at small scales. It is interesting to point out here that the density and velocity structures of the Ursa Major cirrus are clearly anisotropic; filaments with an aspect ratio of 15 are observed. One important step in characterising interstellar turbulence would be to quantify this anisotropy and its variation with scale.

It is also interesting to note that the spectral indexes of the HI are significantly different from what is observed with molecular or dust emission. Several studies of integrated CO emission shows spectral indexes around −2.5 and −2.8. For instance Bensch et al. (2001) found relatively uniform spectral index values ($-2.8 < \beta < -2.5$) for a set of five molecular clouds observed with tracers of different optical depth (^{12}CO and ^{13}CO $J = 1 \rightarrow 0$). The work of Gautier et al. (1992) on 100 μm dust emission also shows a relatively shallow slope $\beta \sim -3$ for non-starforming regions. These results seem to indicate more small scale structures than are observed in HI. However molecular emission is, contrary to HI, strongly affected by opacity and heating variations within the cloud which may significantly modify the power spectrum. Similarly the dust thermal emission may vary locally according to the grain

properties (Miville-Deschênes et al. 2002), to the extinction of the stellar radiation or the abundance of H_2. This apparent difference between the atomic and molecular gas structure clearly deserves further analysis.

7. Conclusion

We have presented a power spectrum analysis of 21 cm interferometric observations of the Ursa Major / North Celestial Loop region. These observations of an isolated high-latitude region, with no star-formation activity, allow us to study the statistical properties of the inertial range cascade of interstellar turbulence in the HI gas. From the analysis of the integrated emission, of velocity channels and of the centroid velocity field of the HI emission with a few assumptions on the depth of the emitting medium and its transparency, we were able to estimate the spectral indexes of the density and velocity fields in 3-D. For both fields we find a spectral index of -3.6 ± 0.2 over almost three orders of magnitudes in scales. The velocity field and the integrated emission map show moderate correlation with a value of at most 0.4 in the Ursa Major field.

Acknowledgements. The authors thank the team at the DRAO observatory for their help in the data reduction and Snezana Stanimirovic for very useful comments. The Fond FCAR du Québec and the National Science and Engineering Research Council of Canada provided funds to support this research project.

References

Baars, J. W. M., Genzel, R., Pauliny-Toth, I. I. K., & Witzel, A. 1977, A&A, 61, 99
Bensch, F., Stutzki, J., & Ossenkopf, V. 2001, A&A, 366, 636
Burton, W. B., & Hartmann, D. 1994, Ap&SS, 217, 189
Chandrasekhar, S. 1949, ApJ, 110, 329
Cho, J., Lazarian, A., & Vishniac, E. T. 2003, in Turbulence and Magnetic Fields in Astrophysics, ed. E. Falgarone, & T. Passot (Springer LNP), 56
Crovisier, J., & Dickey, J. M. 1983, A&A, 122, 282
Deshpande, A. A., Dwarakanath, K. S., & Goss, W. M. 2000, ApJ, 543, 227
Dickey, J. M., McClure-Griffiths, N. M., Stanimirovic, S., Gaensler, B. M., & Green, A. J. 2001, ApJ, 561, 264
Elmegreen, B. G., Kim, S., & Staveley-Smith, L. 2001, ApJ, 548, 749
Falgarone, E., & Phillips, T. G. 1990, ApJ, 359, 344
Falgarone, E., & Puget, J. L. 1995, A&A, 293, 840
Falgarone, E., Phillips, T. G., & Walker, C. K. 1991, ApJ, 378, 186
Falgarone, E., Pineau Des Forêts, G., & Roueff, E. 1995, A&A, 300, 870
Gautier, T. N. I., Boulanger, F., Pérault, M., & Puget, J. L. 1992, AJ, 103, 1313
Gibson, S. J., Taylor, A. R., Higgs, L. A., & Dewdney, P. E. 2000, ApJ, 540, 851
Godbout, S., Joncas, G., Durand, D., & Arsenault, R. 1997, ApJ, 478, 271
Goldman, I. 2000, ApJ, 541, 701
Lazarian, A., Pogosyan, D. Goldreich, P., & Sridhar, S. 1995, ApJ, 438, 763
Green, D. A. 1993, MNRAS, 262, 327
Heiles, C. 1989, ApJ, 336, 808
Heitsch, F., Mac Low, M. M., & Klessen, R. S. 2001, ApJ, 547, 280
Joncas, G., & Roy, J. R. 1986, ApJ, 307, 649
Joncas, G., Boulanger, F., & Dewdney, P. E. 1992, ApJ, 397, 165
Joulain, K., Falgarone, E., Pineau Des Forêts, G., & Flower, D. 1998, A&A, 340, 241
Kolmogorov, A. N. 1941, Dokl. Akad. Nauk. SSSR, 30, 299
Kulkarni, S. R., & Heiles, C. 1987, In Interstellar processes, ed. D. J. Hollenbach, & H. A. Thronson, Jr. (Dordrecht: Reidel), 87
Landecker, T. L., Dewdney, P. E., Burgess, T. A., et al. 2000, A&AS, 145, 509
Lazarian, A., & Pogosyan, D. 2000, ApJ, 537, 720
Lazarian, A., Pogosyan, D., Vázquez-Semadeni, E., & Pichardo, B. 2001, ApJ, 555, 130
Lockman, F. J., & Gehman, C. S. 1991, ApJ, 382, L182
Low, F. J., Young, E., Beintema, D. A., et al. 1984, ApJ, 278, L19
Mac Low, M. M. 1999, ApJ, 524, 169
Magnani, L., Caillault, J. P., & Armus, L. 1990, ApJ, 357, 602
Meyerdierks, H., Heithausen, A., & Reif, K. 1991, A&A, 245, 247
Miesch, M. S., Scalo, J., & Bally, J. 1999, ApJ, 524, 895
Miville-Deschênes, M. A., Joncas, G., & Durand, D. 1995, ApJ, 454, 316
Miville-Deschênes, M. A., Boulanger, F., Joncas, G., & Falgarone, E. 2002, A&A, 381, 209
Miville-Deschênes, M. A., Levrier, F., & Falgarone, E. 2003, ApJ, 593, 831
O'Dell, C. R. 1986, ApJ, 304, 767
Ostriker, E. C., Stone, J. M., & Gammie, C. F. 2001, ApJ, 546, 980
Padoan, P., & Nordlund, A. 1999, ApJ, 526, 279
Penprase, B. E. 1993, ApJS, 88, 433
Pety, J. 1999, Structures dissipatives de la turbulence interstellaire: signatures cinématiques, Ph.D. Thesis, Université Paris 6
Porter, D. H., Pouquet, A., & Woodward, P. R. 1994, Phys. Fluids, 6, 2133
Pound, M. W., & Goodman, A. A. 1997, ApJ, 482, 334
Scalo, J., & Chappell, D. 1999, ApJ, 510, 258
Spicker, J., & Feitzinger, J. V. 1988a, A&A, 191, 10
Stanimirovic, S., & Lazarian, A. 2001, ApJ, 551, L53
Stanimirovic, S., Staveley-Smith, L., Dickey, J. M., Sault, R. J., & Snowden, S. L. 1999, MNRAS, 302, 417
Starck, J. L., & Murtagh, F. 1998, PASP, 110, 193
Stone, J. M., Ostriker, E. C., & Gammie, C. F. 1998, ApJ, 508, L99
Stutzki, J., Bensch, F., Heithausen, A., Ossenkopf, V., & Zielinsky, M. 1998, A&A, 336, 697
Taylor, A. R., Gibson, S. J., Peracaula, M., et al. 2003, AJ, 125, 3145
Tennekes, H., & Lumley, J. L. 1972, A First Course in Turbulence (Cambridge: MIT Press)
von Weizsäcker, C. F. 1951, ApJ, 114, 165